Turbulence Measurements from Compliant Moorings. Part II: Motion Correction

LEVI F. KILCHER

National Renewable Energy Laboratory, Golden, Colorado

JIM THOMSON

Applied Physics Laboratory, University of Washington, Seattle, Washington

SAMUEL HARDING

Pacific Northwest National Laboratory, Richland, Washington

SVEN NYLUND

Nortek AS, Rud, Norway

(Manuscript received 1 November 2016, in final form 25 February 2017)

ABSTRACT

Acoustic Doppler velocimeters (ADVs) are a valuable tool for making high-precision measurements of turbulence, and moorings are a convenient and ubiquitous platform for making many kinds of measurements in the ocean. However, because of concerns that mooring motion can contaminate turbulence measurements and that acoustic Doppler profilers make middepth velocity measurements relatively easy, ADVs are not frequently deployed from moorings. This work demonstrates that inertial motion measurements can be used to reduce motion contamination from moored ADV velocity measurements. Three distinct mooring platforms were deployed in a tidal channel with inertial-motion-sensor-equipped ADVs. In each case, motion correction based on the inertial measurements reduces mooring motion contamination of velocity measurements. The spectra from these measurements are consistent with other measurements in tidal channels and have an $f^{-5/3}$ slope at high frequencies—consistent with Kolmogorov's theory of isotropic turbulence. Motion correction also improves estimates of cross spectra and Reynolds stresses. A comparison of turbulence dissipation with flow speed and turbulence production indicates a bottom boundary layer production–dissipation balance during ebb and flood that is consistent with the strong tidal forcing at the site. These results indicate that inertial-motion-sensor-equipped ADVs are a valuable new tool for making high-precision turbulence measurements from moorings.

1. Introduction

Acoustic Doppler velocimeters (ADVs) have been used to make high-precision measurements of water velocity for over 20 years (Kraus et al. 1994; Lohrmann et al. 1995). During that time, they have been deployed around the world to measure turbulence from a range of platforms, including in the laboratory setting (Voulgaris and Trowbridge 1998); from stationary structures on ocean, river, and lake bottoms (Kim et al. 2000; Lorke 2007; Cartwright et al. 2009); in surface waters from a pole lowered from a ship's bow (Geyer et al. 2008); and in the deep ocean from autonomous underwater vehicles (e.g., Zhang et al. 2001; Goodman et al. 2006).

A relatively small fraction of ADV measurements have been made from moorings (e.g., Fer and Paskyabi 2014). Presumably this is because mooring motion can contaminate ADV measurements, and acoustic Doppler profilers (ADPs) can measure some middepth turbulence statistics without a mooring (e.g., Stacey et al. 1999a; Rippeth et al. 2002; Wiles et al. 2006; Guerra Paris and Thomson 2017). Still, ADV measurements have distinct characteristics that can be advantageous: they are capable of higher sample rates, have higher

Denotes content that is immediately available upon publication as open access.

Corresponding author: Levi Kilcher, levi.kilcher@nrel.gov

DOI: 10.1175/JTECH-D-16-0213.1

signal-to-noise ratios, and have a much smaller sample volume (1 cm, as opposed to several meters).

Inertial motion unit (IMU) sensors have been used in the aerospace and aeronautical industries to quantify the motion of a wide range of systems, and to improve atmospheric velocity measurements, for several decades (Axford 1968; Edson et al. 1998; Bevly 2004). In the last decade, the smartphone, drone, and ''Internet of Things'' markets have driven innovation in microelectrical–mechanical systems, including the IMU. As a result of this growth and innovation, the cost, power requirements, and size of IMUs have come down. These changes have allowed these sensors to be integrated into oceanographic instruments that have small form factors, and rely on battery power.

Nortek now offers a version of their Vector ADV with a MicroStrain 3DM-GX3-25 IMU sensor (Nortek 2005; MicroStrain 2012). The IMU's signals are incorporated into the Vector ADV's data stream so that its motion and orientation signals are tightly synchronized with the ADV's velocity measurements. This tight synchronization provides a dataset that can be utilized to quantify ADV motion in Earth's inertial reference frame and to remove that motion from the ADV's velocity measurements at each time step of its sampling (Edson et al. 1998). This work utilizes ''ADV-IMU'' measurements from middepth moorings in Puget Sound to demonstrate that motion correction can improve the accuracy of oceanic turbulence spectra, turbulence dissipation, and Reynolds stress estimates.

This effort was originally motivated by a need for low-cost, high-precision turbulence measurements for the emerging tidal energy industry (McCaffrey et al. 2015; Alexander and Hamlington 2015). Experience in the wind energy industry has shown that wind turbine lifetimes are reduced by atmospheric turbulence, and the same is expected to be true for tidal energy turbines. In the atmosphere, meteorological towers are often used to position sonic anemometers at the hub height of wind turbines for measuring detailed turbulence inflow statistics (Hand et al. 2003; Kelley et al. 2005; Mücke et al. 2011; Afgan et al. 2013). In the ocean, tower-mounted hub-height turbulence measurements have been made, but they are challenging to install and maintain in energetic tidal sites (Gunawan et al. 2014; Thomson et al. 2012). Therefore, the U.S. Department of Energy funded this work to investigate the accuracy of mooring-deployed ADV-IMUs to reduce the cost of turbulence measurements at tidal energy sites (Kilcher et al. 2016). The approach proved to be successful and potentially useful to the broader oceanographic community interested in moored turbulence measurements (Lueck and Huang 1999; Doherty et al. 1999; Nash et al. 2004; Perlin and Moum 2012; Alford 2010; Paskyabi and Fer 2013).

The next section describes details of the measurements, including a summary of the hardware configurations (platforms) that were used to support and position the ADV-IMUs in the water column. A detailed description of the motion of these platforms is found in the companion paper to this work, Harding et al. (2017, hereafter Part I). Section 3 describes the mathematical details of motion correction, and section 4 presents results from applying the method to measurements from the various platforms. Section 5 is a discussion of the energetics of the tidal channel in which the measurements were made and demonstrates that the measurements are consistent with turbulence theory and other measurements in similar regimes. A summary and concluding remarks are provided in section 6.

2. Measurements

This work focuses on measuring turbulence from ADVs that are equipped with IMUs and deployed from moving (moored) platforms. The ADVs utilized for these measurements were Nortek Vector ADVs equipped with MicroStrain 3DM-GX3-25 IMUs. These IMUs captured all six components of ADV motion (three components of angular rotation and three components of linear acceleration), as well as the orientation of the ADV pressure case. The IMU measures its motion at 1 kHz and uses internal signal integration (Kalman filtering) to output the motion signals at the same sample rate as the ADV's velocity measurements (the measurements are synchronized to within 10^{-2} s). This reduces aliasing of the IMU's motion measurements above the ADV's sample rate (MicroStrain 2010).

All measurements used in this work were made in Admiralty Inlet, Washington, approximately 500 m west-southwest of Admiralty Head in 60 m of water at 48°9.18′N, 122°41.22′W (Fig. 1). The site is approximately 6 km east of Port Townsend, Washington. Admiralty Inlet is the largest waterway connecting Puget Sound to the Strait of Juan de Fuca, and it possesses a large semidiurnal tidal flow (Thomson et al. 2012; Polagye and Thomson 2013). This work utilizes data from three distinct deployment platforms: the Tidal Turbulence Mooring, a StableMoor buoy, and a sounding weight. All data used in this analysis are available from the Marine and Hydrokinetic Data Repository (http://mhkdr.openei.org; submission IDs: 49, 50, and 51). Each of these platforms is briefly described below, and additional details, photographs, and schematic diagrams can be found in Part I. This entire work—including manuscript source text, source data, figures, and analysis scripts—is publicly available (Kilcher et al. 2017).

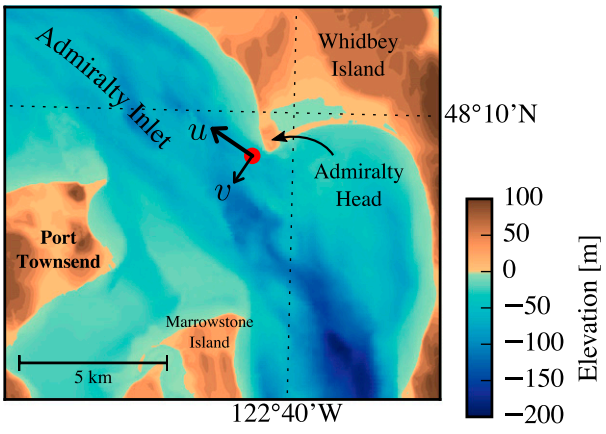

FIG. 1. Bathymetry of Admiralty Inlet near Port Townsend (Finlayson 2005). The red dot indicates the location of all measurements. Positive u direction is the direction of ebb flow (thick arrow originating from red dot), and positive v is away from Admiralty Head (smaller arrow).

a. *Tidal Turbulence Mooring*

The Tidal Turbulence Mooring (TTM) system is a simple mooring system with a strongback fin suspended between a steel clump-weight anchor weighing 1200 kg when dry and a 0.93-m-diameter spherical steel buoy with a buoyancy of 320 kg. The ADV pressure cases were clamped to one side of the strongback fin and the ADV sensor head was positioned 10 cm in front of the fin's leading edge (Fig. 2). The leading edge of the fin is fastened in-line with the mooring line. This configuration was designed to work like a weather vane, such that the drag on the fin held the ADV head upstream of the mooring components. This work utilizes data from two TTM deployments.

The first TTM deployment was from 1730 local time (LT) 12 June 2012 until 1430 LT 14 June 2012. Two Nortek ADVs were clamped to either side of the fin so that the axis of their cylindrical pressure cases were parallel with the leading edge of the strongback. The ADV heads were spaced 0.5 m apart vertically along the fin. Only one of these ADVs was equipped with an integrated IMU. This TTM also had an upward-looking ADP mounted on the mooring anchor.

Periods of time during which this mooring interfered with a beam of the ADP were identified by inspecting the profiler's acoustic amplitude signal. Periods during which one beam of the profiler had >5% higher acoustic amplitude than the other beams were flagged as "contaminated" and excluded from averaging. Five-minute averages in which more than 50% of the data were contaminated in this way were masked as invalid.

The second TTM deployment was from 0600 LT 17 June 2014 to 0500 LT 19 June 2014. Two Nortek ADV-IMUs were mounted on this TTM, with their heads spaced 0.5 m apart along the fin. In this case, the

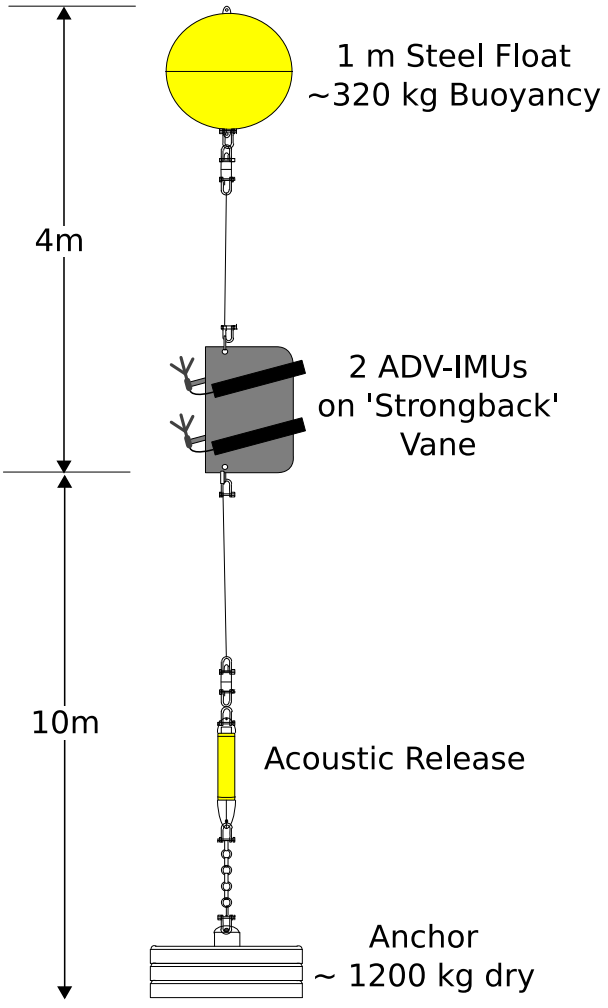

FIG. 2. Schematic diagram of the TTM (not to scale). A pop-up buoy for anchor recovery is not shown, for simplicity.

pressure cases and ADV heads were inclined at an angle of 18° from normal to the leading edge of the fin to account for mooring blowdown during strong currents (Fig. 3). This change was made to reduce vibrational motion observed during the June 2012 deployment that was believed to be associated with the orientation of the pressure cases. There was no ADP on the anchor of this TTM.

b. *The StableMoor platform*

The second deployment platform was a cylindrical StableMoor syntactic foam buoy (manufacturer: DeepWater Buoyancy, Inc.) that was anchored to a clump weight that weighed 1200 kg (Fig. 4). The buoy is 3.5 m long and 0.45 m in diameter with a tail ring that is 0.76 m in diameter. The StableMoor buoy (SMB) weighs 295 kg in air and has a buoyancy of 185 kg in water.

The SMB was deployed with an ADV-IMU mounted at its nose from 1121 LT 12 May to 1153 LT 13 May 2015.

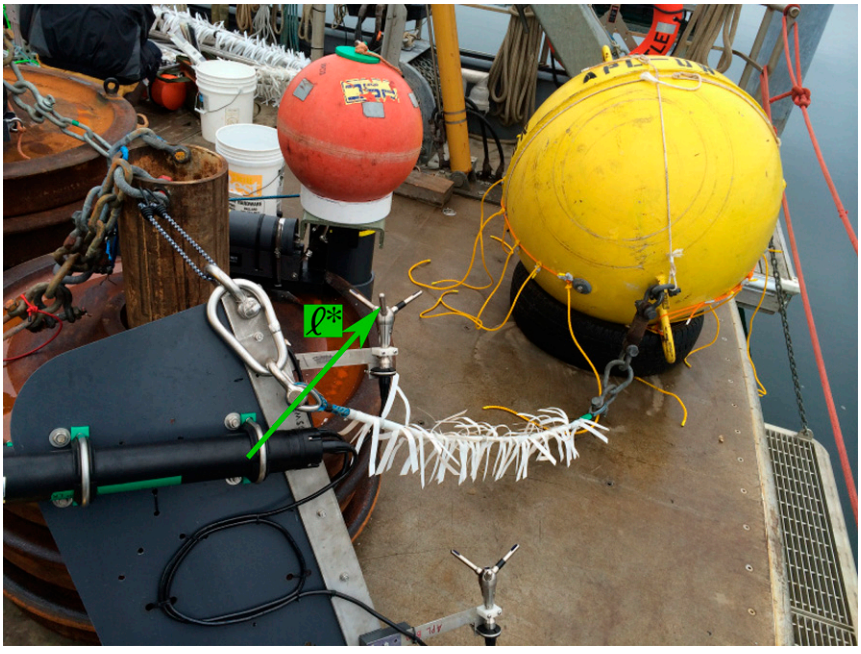

FIG. 3. TTM components on the deck of the R/V *Jack Robertson*. The TTM includes two ADVs, with pressure cases mounted on opposite sides of the fin. The anchor stack includes a pop-up buoy for retrieval. The green arrow indicates the vector from the IMU to the ADV head (face of the transmit transducer).

The sample volume of the ADV is 10 cm forward of the nose and 20 cm above the center line of the SMB (Fig. 4). Based on Wyngaard et al.'s (1985) investigation of a similarly shaped slender body, the velocity measurements should have flow-distortion effects of less than 10%. The SMB was equipped with a 1200-kHz Teledyne RD Instruments (RDI) Workhorse Sentinel ADP that was oriented downward looking to measure water velocity below the platform in twelve 1-m bins and to measure platform motion ("bottom tracking"), all at a 1-Hz sample rate.

The SMB has two primary advantages compared to the TTM. First, it is significantly more massive and hydrodynamically stable than the TTM, which reduces the frequency of motions of the platform (Part I). Second, the SMB is capable of supporting a bottom-tracking ADP, which provides an independent measure of the platform's translational motion. Disadvantages of the SMB include its size, which adds to the challenge of deployment and recovery, and its cost, which is significantly higher than the TTM system.

c. Turbulence torpedo

The turbulence torpedo is a simple sounding weight with an ADV head mounted forward of the nose and the ADV pressure case strapped below (Fig. 5). This platform was deployed on 14 May 2015, for 37 min starting at 0741 LT. This measurement was made from a davit that hung the system from the side of the ship to a depth of approximately 25 m. The primary advantages of this platform are its compact size, low cost, and flexibility to perform spatial transects.

d. Coordinate system and turbulence averaging

Unless stated otherwise, vector quantities in this work are in a fixed "principal axes" coordinate system that is aligned with the bidirectional tidal flow: positive u is in the direction of ebb (310°T), positive w is vertically upward, and v is the cross-stream component in a right-handed coordinate system (Fig. 1). The full velocity vector, $\tilde{\mathbf{u}} = (\tilde{u}, \tilde{v}, \tilde{w})$, is separated into mean and turbulent components as $\tilde{\mathbf{u}} = \overline{\mathbf{u}} + \mathbf{u}$, where the overbar denotes a 5-min average. Turbulence kinetic energy, $\mathrm{TKE} = \overline{u^2} + \overline{v^2} + \overline{w^2}$, and Reynolds stresses, $\overline{uv}$, $\overline{uw}$, $\overline{vw}$, are also estimated using a 5-min average. The horizontal velocity magnitude is computed as $\overline{U} = (\overline{u}^2 + \overline{v}^2)^{1/2}$. The friction velocity is estimated as $u_* = (\overline{uw}^2 + \overline{vw}^2)^{1/4}$; note that this is taken at the height of the ADV measurements and should therefore only be interpreted as a proxy for the friction velocity at the bottom boundary.

All spectra, $S\{x\}(f) = |\mathcal{F}\{x(t)\}|^2$, and cross spectra, $C\{x, y\}(f) = \mathrm{real}(\mathcal{F}\{x(t)\}.\mathcal{F}\{y(t)\})$, are computed using NumPy fast Fourier transform routines (van der Walt et al. 2011). Here, $\mathcal{F}\{x(t)\}$ denotes the fast Fourier transform of a signal $x(t)$ that has been linearly

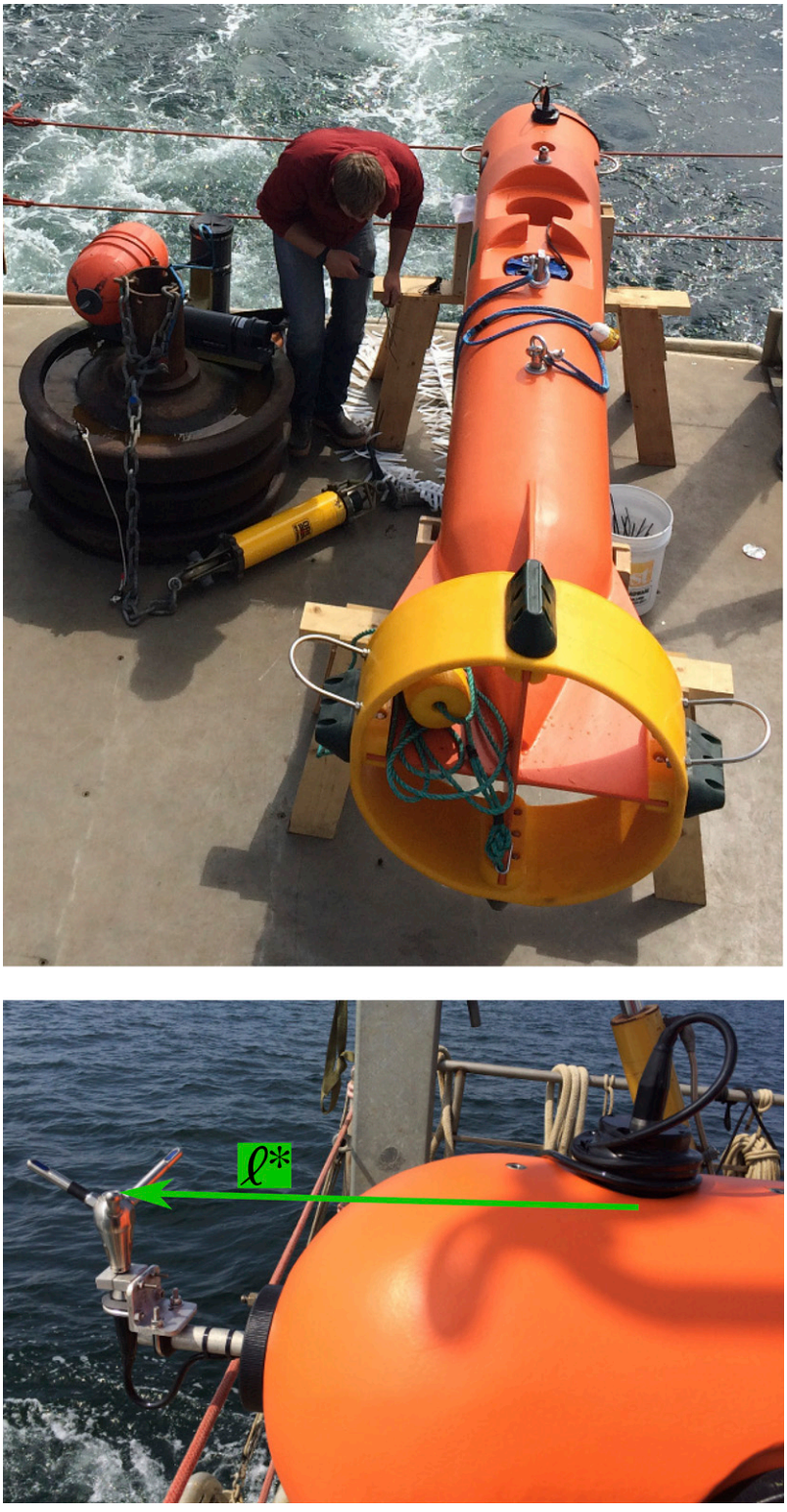

FIG. 4. (top) Alex DeKlerk checks to ensure that the SMB buoy is properly fastened to its anchor; the RDI workhorse ADP can be seen in the rear instrument bay. A bridle is draped across the top of the buoy for deployment and recovery, and a small marker buoy fastened to the tail is useful during recovery. (bottom) Close-up of the SMB buoy with the ADV head and the top of its pressure case. The green arrow indicates the vector from the IMU to the ADV head.

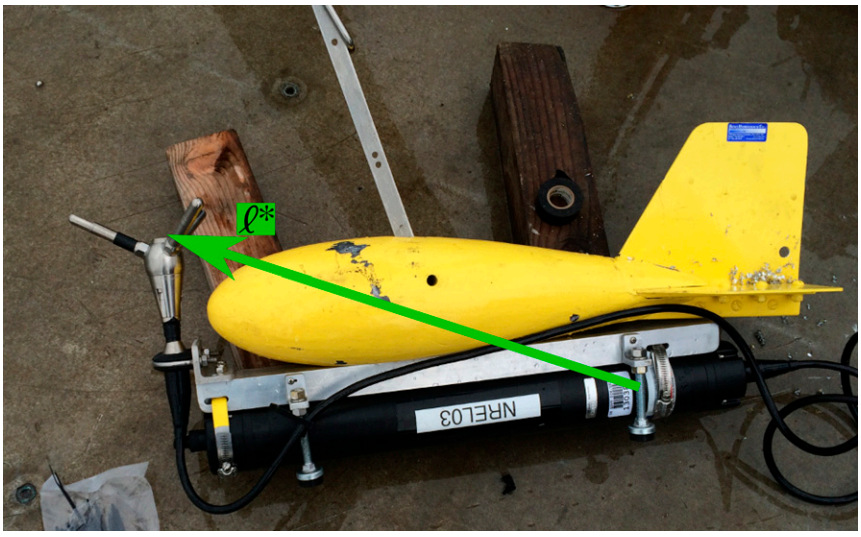

FIG. 5. The turbulence platform showing details of the ADV head and pressure case configuration. The green arrow indicates the vector from the IMU to the ADV head. The head cable was taped out of the way beneath the sounding-weight tail fins shortly after this photograph was taken.

detrended and Hanning windowed to reduce spectral reddening.

Throughout the remainder of this work, the dependence of S and C on f is implied (e.g., $S\{x\}(f)$ is hereinafter $S\{x\}$), and for other variables the dependence on t is implied. Spectra and cross spectra are normalized to preserve variance, for example, $\int S\{u\}\,df = \overline{u^2}$ and $\int C\{u, v\}\,df = \overline{uv}$, respectively. The notations $S\{\mathbf{u}\} = (S\{u\}, S\{v\}, S\{w\})$ and $C\{\mathbf{u}\} = (C\{u, v\}, C\{u, w\}, C\{v, w\})$ denote the set of spectra and cross spectra for each velocity component and pairs of components, respectively.

Turbulence dissipation rates are computed as

$$\varepsilon = \frac{1}{\overline{U}}\left(\alpha\left\langle (S\{u\} + S\{v\} + S\{w\})f^{5/3}\right\rangle_{f_{\mathrm{IS}}}\right)^{3/2}, \qquad (1)$$

where $\alpha = 0.5$ and $\langle\,\rangle_{f_{\mathrm{IS}}}$ denote an average over the inertial subrange of the velocity spectra and where the signal-to-noise ratio is small (Lumley and Terray 1983; Sreenivasan 1995). Throughout this work, we take this average from 0.3 to 1 Hz for the u and v components, and 0.3 to 3 Hz for the w component.

3. Methodology

This work describes a method for correcting velocity measurements from a moving velocity sensor $\tilde{\mathbf{u}}_m$ using independent measurements of that sensor's motion $\tilde{\mathbf{u}}_h$ to remove the motion from the velocity measurements and thus estimate the "motion-corrected velocity":

$$\tilde{\mathbf{u}}(t) = \tilde{\mathbf{u}}_m(t) + \tilde{\mathbf{u}}_h(t). \qquad (2)$$

Note here that the plus sign (+) is correct because head motion, $\tilde{\mathbf{u}}_h$, induces a measured velocity in the opposite direction of the head motion itself ($\tilde{\mathbf{u}}_m = \tilde{\mathbf{u}} - \tilde{\mathbf{u}}_h$). This approach has been used to successfully correct sonic anemometer measurements of atmospheric turbulence (e.g., Edson et al. 1998; Miller et al. 2008). In the ocean, previous works have utilized IMUs to quantify the motion of multiscale profilers for the purpose of measuring the full spectrum of oceanic shear (Winkel et al. 1996) and to quantify the motion of thermistor sensors (Moum and Nash 2009), but the Edson et al. (1998) approach has not been documented for moored ADV measurements.

The MicroStrain IMU available in the Nortek Vector ADV measures the linear acceleration $\mathbf{a}^*(t)$, rotational motion $\boldsymbol{\omega}^*(t)$, and orientation matrix in the Earth reference frame, $\mathbf{R}(t)$, of the ADV at every time step of the ADV's sampling. The asterisk superscripts denote that these vectors are measured in the ADV's local coordinate system. They can be rotated into the Earth frame using the inverse of the orientation matrix: $\mathbf{a}(t) = \mathbf{R}^{\mathrm{T}}(t) \cdot \mathbf{a}^*(t)$. The motion of the ADV head is calculated from these signals as the sum of rotational and translational motion,

$$\begin{aligned}\tilde{\mathbf{u}}_h &= \tilde{\mathbf{u}}_{\boldsymbol{\omega}} + \tilde{\mathbf{u}}_{\mathbf{a}} + \tilde{\mathbf{u}}_{\mathrm{low}} \\ &= \mathbf{R}^{\mathrm{T}} \cdot [\boldsymbol{\omega}^*(t) \times \boldsymbol{\ell}^*] + \int \rangle \mathbf{a}(t) \langle_{f_{\mathbf{a}}} dt + \tilde{\mathbf{u}}_{\mathrm{low}}. \end{aligned} \qquad (3)$$

Here, $\boldsymbol{\ell}^*$ is the vector from the IMU to the ADV head and the notation $\rangle \cdot \langle_{f_{\mathbf{a}}}$ indicates a high-pass filtering

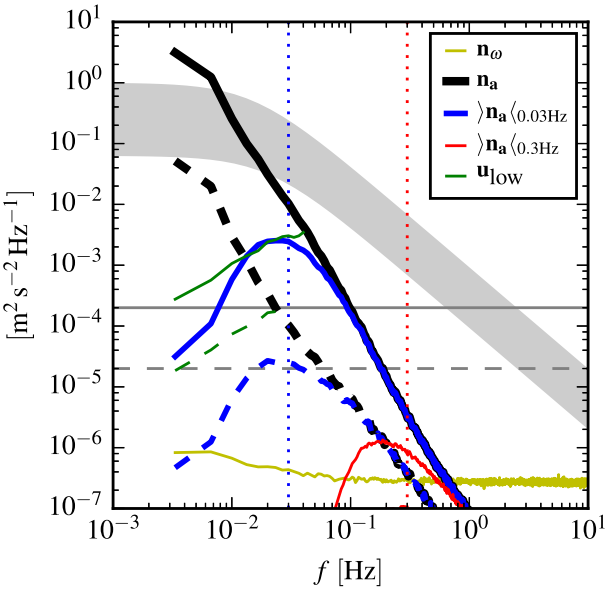

FIG. 6. The spectral noise levels of rotational velocity ($S\{\mathbf{n}_\omega\}$, yellow) and translational velocity ($S\{\mathbf{n}_\mathbf{a}\}$, black) estimated from an ADV-IMU resting motionless on a table. Solid and dashed lines indicate the horizontal and vertical components, respectively, of $S\{\mathbf{n}_\mathbf{a}\}$ and $S\{\mathbf{u}_{low}\}$. The $\mathbf{n}_\mathbf{a}$ signals are unfiltered (black) and high-pass filtered at 0.03 (blue) and 0.3 Hz (red); vertical dotted lines indicate the filter frequency. Green lines are an estimate of $\mathbf{u}_{low}$ for the TTM. Gray horizontal lines indicate the horizontal (solid) and vertical (dashed) ADV noise levels. The shaded region indicates the range of $S\{\mathbf{u}\}$ presented in the next section.

operation at frequency $f_\mathbf{a}$. The high-pass filter reduces low-frequency noise in **a**—sometimes referred to as bias drift—that is amplified by integration (Barshan and Durrant-Whyte 1995; Bevly 2004; Gulmammadov 2009). Term $\tilde{\mathbf{u}}_{low}$ is the low-frequency translational motion that is unresolved by $\tilde{\mathbf{u}}_\mathbf{a}$, and it is discussed in more detail below. To avoid double counting, $\tilde{\mathbf{u}}_{low}$ should be estimated by applying the complementary low-pass filter (i.e., at $f_\mathbf{a}$) to the independent measurement of low-frequency motion. We use fourth-order zero-phase (bidirectional) Hanning filters for all filtering operations.

The noise levels of the IMU, $\mathbf{n}_\omega$ and $\mathbf{n}_\mathbf{a}$, are computed from ADV-IMU data collected while the instrument was resting motionless on a table for several hours, where, for this motionless dataset, the noise levels are defined according to (3) with $\mathbf{n}_\omega$ in place of $\tilde{\mathbf{u}}_\omega$ and $\mathbf{n}_\mathbf{a}$ in place of $\tilde{\mathbf{u}}_\mathbf{a}$.

For quantifying $\mathbf{n}_\omega$ we assume that $|\ell^*| = 1$, which is the approximate length of the ADV head cable. Term $S\{\mathbf{n}_\omega\}$ is equal in all three components, because the rotation-rate sensor noise levels are independent of orientation (Fig. 6, yellow). Term $S\{\mathbf{n}_\omega\}$ is several orders of magnitude lower than the velocity spectra we measured (gray region), and also more than an order of magnitude smaller than the Doppler noise levels of the ADV. This indicates that the precision of $\tilde{\mathbf{u}}_\omega$ (i.e., the angular rate sensor) is adequate for making corrections to ADV velocity measurements.

The IMU's translational noise level $S\{\mathbf{n}_\mathbf{a}\}$ (Fig. 6, black), on the other hand, is dominated by an f^{-2} slope that results from integrating the low-frequency noise in **a**. The horizontal (u and v) spectra of these noise levels are identical, and so we present only one of them for simplicity (solid lines). The vertical spectra noise levels are different because the signal-to-noise ratio is larger (dashed black lines). High-pass filtering reduces the low-frequency noise (blue and red) so that it does not contaminate motion correction, but any real motion that does exist at these frequencies is lost (Egeland 2014; VanZwieten et al. 2015). This means there is a residual low-frequency translational motion $\tilde{\mathbf{u}}_{low}$ that needs to be measured independently—or at the very least considered—when using ADV-IMU data from moving platforms.

For the SMB, the ADP bottom-track measured $\tilde{\mathbf{u}}_{low}$ and this measurement agree with $\tilde{\mathbf{u}}_\mathbf{a}$ over a narrow frequency band (see Part I, appendix A), indicating that the ADP and IMU are resolving the same motion. When this is the case, it is trivial to select a frequency in the middle of the spectral overlap (in this case, we choose $f_\mathbf{a} = 0.2$ Hz), and high-pass and low-pass filter $\tilde{\mathbf{u}}_\mathbf{a}$ and $\tilde{\mathbf{u}}_{low}$, respectively, then sum to estimate the total translational motion.

The position of the TTM ADV can be estimated, relative to its anchor, by assuming the mooring acts like a rigid pole and using the IMU orientation matrix to estimate the pole's "lean." The position obtained from this model can then be differentiated to estimate $\tilde{\mathbf{u}}_{low}$ (this model does not apply at high frequencies). Spectra of $\tilde{\mathbf{u}}_{low}$ estimated using this approach for the June 2014 TTM deployment (Fig. 6, green) are plotted up to the point where they cross their respective $S\{\tilde{\mathbf{u}}_\mathbf{a}\}$ noise level (black). Together, these two lines provide an "aggregate noise level" of translational velocity estimates for the TTM: the rigid pole estimate of $\tilde{\mathbf{u}}_{low}$ indicates the amplitude of unresolved motion at low f (green) and $S\{\tilde{\mathbf{u}}_\mathbf{a}\}$ indicates the limits of the IMU at high f (black). Coincidentally, $S\{\langle \mathbf{n}_\mathbf{a} \rangle_{0.03Hz}\}$ (blue) is not a terrible approximation for this aggregate noise level. Furthermore, because this aggregate noise level is smaller by at least a factor of 4 than the velocity sprectra that we measured (shaded region), the results of motion correction are insensitive to whether we use the rigid pole model to estimate $\tilde{\mathbf{u}}_{low}$ or we simply assume that $\tilde{\mathbf{u}}_{low} = 0$.

The choice of $f_\mathbf{a}$ does influence the effectiveness of motion correction (Fig. 7). When $f_\mathbf{a}$ is too high (e.g., 0.3 Hz, red), the high-pass filter removes resolved motion

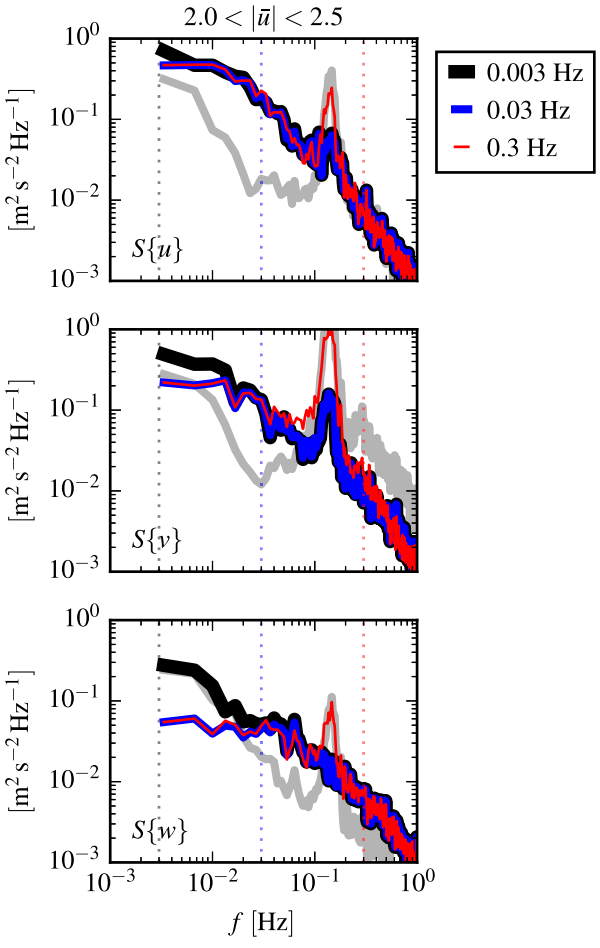

FIG. 7. Motion-corrected velocity spectra $S\{\mathbf{u}\}$ for a range of high-pass filter frequencies: $f_a = 0.3$ Hz (thin red), 0.03 Hz (blue), and 0.003 Hz (thick black). The vertical dotted lines indicate the filter frequency. The thick gray line is $S\{\mathbf{u}_h\}$ for $f_a =$ 0.003 Hz. The data are from the June 2014 TTM deployment when $2.0 < |\bar{u}| < 2.5$ m s^{-1}.

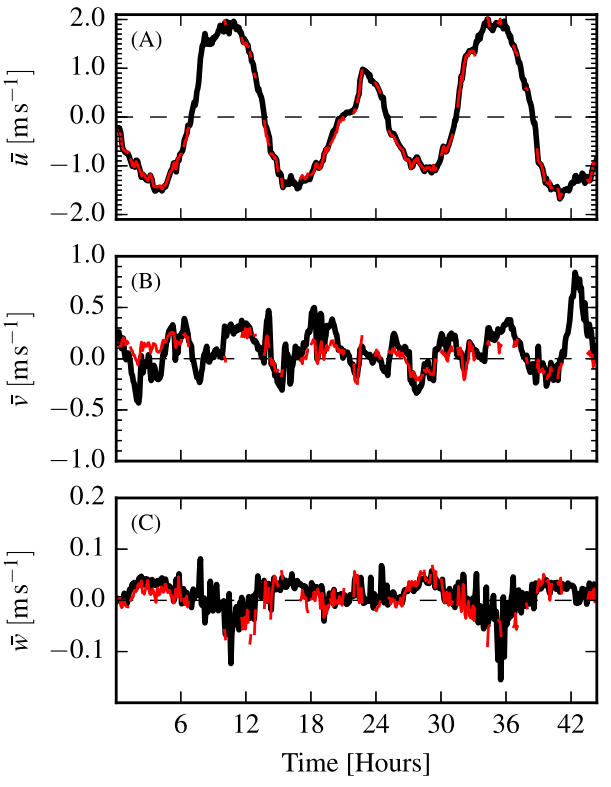

FIG. 8. Time series of tidal velocity in June 2012 at Admiralty Head from ADV-IMU measurements (black), and an ADP on the anchor (red). Note that the vertical scale on the three axes vary by an order of magnitude; the small ticks in (a) and (b) are equivalent to the ticks in (c).

from $\tilde{\mathbf{u}}_h$ that could be used to correct velocity measurements. In particular, notice that the amplitude of the 0.15-Hz peak—which is clearly the result of motion contamination (gray line)—is reduced significantly when we preserve more $\tilde{\mathbf{u}}_h$ information by reducing the high-pass filter frequency to $f_a = 0.03$ Hz. Further reducing f_a to 0.003 Hz does not reduce the peak further, but it does increase the amplitude of the spectra at low frequency. This low-f increase is the IMU-accelerometer's low-frequency bias drift (Fig. 6) contaminating the velocity measurements. Therefore, we conclude that $f_a = 0.03$ Hz is a convenient "middle" frequency that reduces accelerometer bias drift without destroying the resolved motion of the TTM. The same $f_a = 0.03$-Hz filter was selected, based on a similar analysis, for the turbulence torpedo.

Thus, we find that filter selection involves a trade-off between filtering out the bias drift noise at low frequencies while not filtering out measured motion at high frequencies. In general, this will depend on the dynamics of the platform used to support the ADV, and the intensity of the turbulence being measured. When an independent measurement of $\tilde{\mathbf{u}}_{\text{low}}$ is available, the cross coherence with $\tilde{\mathbf{u}}_a$ can indicate a region of spectral overlap and f_a can be selected at the midpoint. Lacking a reliable estimate of $\tilde{\mathbf{u}}_{\text{low}}$, the value of f_a that produces the lowest TKE estimates is likely the best.

Additional details on motion correction—including a detailed accounting of the distinct coordinate systems of the IMU, ADV pressure case, and ADV head—can be found in Kilcher et al. (2016). Open-source Python tools for performing motion correction of ADV-IMU data—including scripts that write processed data in MATLAB and tabulated formats—are available online (at http://lkilcher.github.io/dolfyn/).

4. Results

a. Mean velocity

Figure 8 shows a comparison of $\bar{\mathbf{u}}$ measured by an ADV-IMU mounted on the TTM to an upward-looking

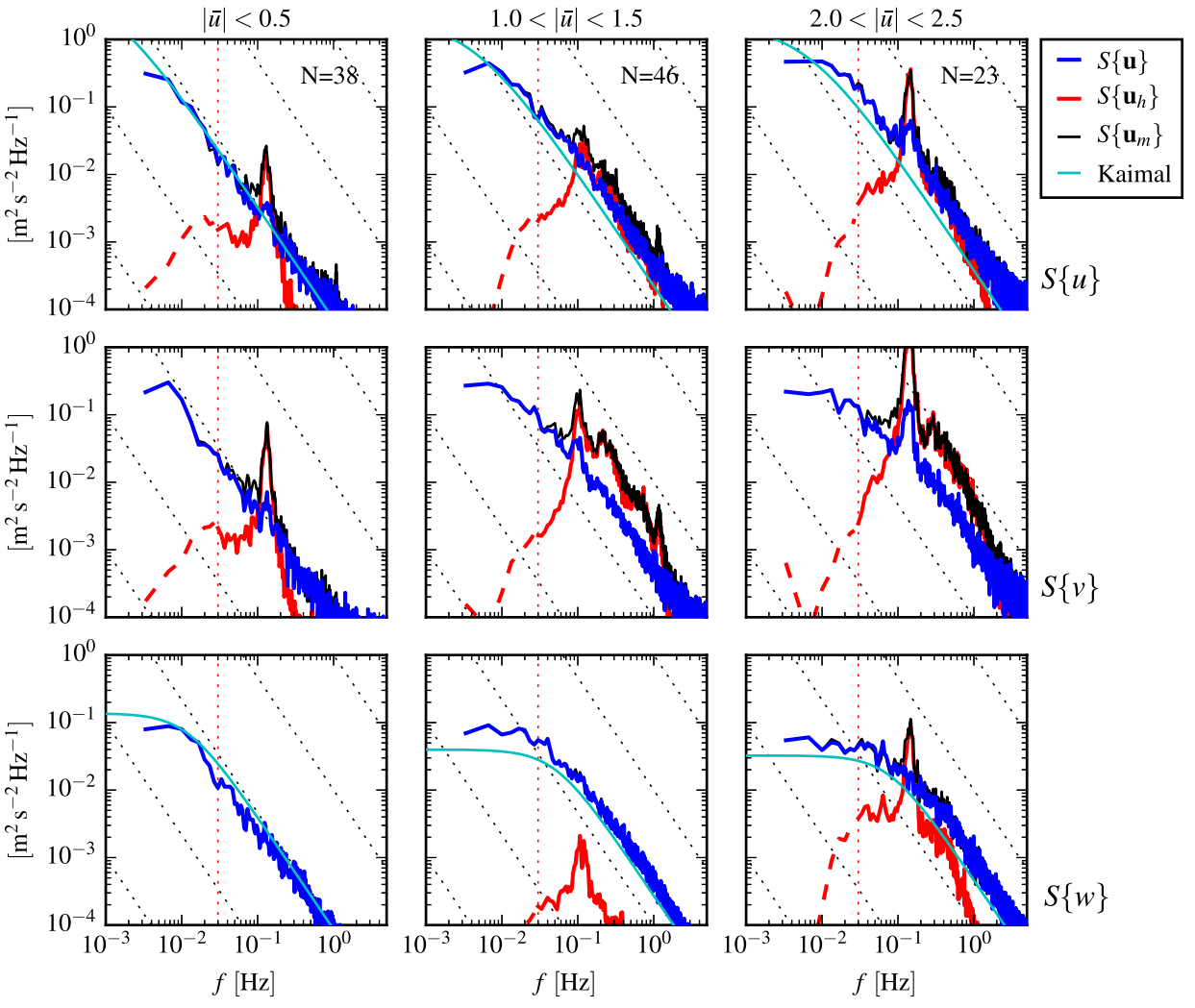

FIG. 9. Turbulence spectra from the June 2014 TTM deployment. Each column is for a range of streamwise velocity magnitudes (indicated at the top in meters per second). The rows are for each component of velocity (indicated at far right). The uncorrected spectra are black, the corrected spectra are blue, and the spectra of ADV head motion is red (also indicated in the legend). The vertical red dotted line indicates f_a for estimating $\mathbf{u}_h$; below this frequency $S\{\mathbf{u}_h\}$ is plotted as a dashed line. Diagonal black dotted lines indicate an $f^{-5/3}$ slope. The cyan line in the first and last rows indicates the semiempirical Kaimal spectrum for the measured values of u_* and $\overline{U}$. The number of spectral ensembles N in each column is indicated in the top row.

ADP on the anchor. The profiler measurements—taken at the same depth as the ADV on the TTM—were contaminated by acoustic reflection from the strongback fin when it was in-line with one of the profiler's beams (see section 2a). When those points (not shown in the figure) are excluded, this comparison shows excellent agreement between the ADV and ADP measurements of mean velocity. The $\overline{u}$, $\overline{v}$, and $\overline{w}$ components have a root-mean-square error of 0.05, 0.13, and 0.03 $\mathrm{m\,s^{-1}}$, respectively. Although it is important to note that there is some discrepancy between ADP- and ADV-measured velocities (especially in $\overline{v}$, which is most likely due to incomplete motion correction), the agreement between the magnitude and direction of these independent velocity measurements indicates that moored ADV-IMUs provide a reliable estimate of mean velocity in the Earth's reference frame.

b. *TTM spectra*

As discussed in detail in Part I, the mooring motion of the TTM $S\{\mathbf{u}_h\}$ has a peak at 0.1–0.2 Hz from swaying of the mooring that is most likely driven by eddy shedding from the spherical buoy (Fig. 9, red lines). There is also higher-frequency broadband motion that is associated with fluttering of the strongback fin around the mooring line. These motions are especially energetic in $S\{v\}$ because this is the direction in which the TTM is most unstable. As is expected from fluid–structure interaction

theory, the amplitude of these motions increases with increasing mean velocity (Morison et al. 1950).

The mooring motion contaminates the uncorrected ADV measurements of velocity $S\{\mathbf{u}_m\}$ whenever the amplitude of the motion is similar to or greater than the amplitude of the turbulence. Fortunately, much of this motion can be removed as detailed in section 3. At high frequencies ($f > 0.3$ Hz) for each mean-flow speed, $S\{\mathbf{u}\}$ is consistent with Kolmogorov's (1941) theory of isotropic turbulence: the spectra decay with an $f^{-5/3}$ slope and have equal amplitude across the velocity components. At lower frequencies, the spectral ''rolloff'' shape is similar to that measured by several others (e.g., Thomson et al. 2012; McMillan et al. 2016). The degree of agreement between Kaimal et al.'s (1972) semiempirical form (cyan) and $S\{\mathbf{u}\}$ is similar to that of Walter et al. (2011). This suggests that bottom boundary layer physics are contributing to the turbulence at this site and depth.

For $|\mathbf{u}| > 1.0\,\mathrm{m\,s^{-1}}$, motion correction improves $S\{u\}$ and $S\{v\}$ at frequencies as high as 3 Hz. This indicates that tight synchronization between the ADV and IMU is important and that implementing asynchronous approaches to motion correction may be challenging.

As successful as motion correction is, some motion contamination is ''persistent.'' This is most notable in $S\{v\}$ at the highest flow speeds ($>2.0\,\mathrm{m\,s^{-1}}$): a peak at 0.15 Hz is an order of magnitude larger than the anticipated spectral shape. This persistent motion contamination is evident to a lesser degree in $S\{u\}$ for $|u| > 2\,\mathrm{m\,s^{-1}}$ and in $S\{v\}$ at lower flow speeds. Term $S\{w\}$ appears to have no persistent motion contamination because the amplitude of the motion in this direction is much lower than the measured spectra.

The amplitude of the persistent motion contamination peaks in $S\{v\}$ at 0.15 Hz is a factor of 5–10 times smaller than the amplitude of the ADV head motion itself. This observation suggests that the MicroStrain IMU can be used to effectively correct mooring motion at this frequency when the amplitude of that motion is less than 5 times the amplitude of the real turbulence spectrum. As a result, we have chosen a value of 3 as a conservative estimate of the motion correction's effectiveness.

In addition to the primary benefit of correcting for mooring motion, the IMU measurements can also be used to identify and screen out persistent motion contamination. For example, one of the most common uses of turbulence spectra is for the calculation of ε and TKE. For these purposes, and based on the relative amplitudes of the 0.15-Hz peaks, we assume that persistent motion contamination is likely where $S\{\mathbf{u}_h\}/S\{\mathbf{u}\} > 3$ and thereby exclude these regions from spectral fits.

In the present case, for u- and w-component spectra, this criterion excludes only a narrow range of frequencies at the 0.15-Hz motion peak for the largest flow speeds. This criterion is more restrictive of v-component spectra at high frequencies for $\overline{U} > 1.0\,\mathrm{m\,s^{-1}}$, but this may be acceptable because the amplitude of $S\{v\}$ at these frequencies—that is, in the isotropic inertial subrange—should be equal to that of $S\{u\}$ and $S\{w\}$ (Kolmogorov 1941).

Agreement of $S\{v\}$ with that of $S\{u\}$ and $S\{w\}$ at frequencies > 0.3 Hz indicates that motion correction is effective at those frequencies even when $S\{\mathbf{u}_h\}/S\{\mathbf{u}\} \gtrsim 3$. This outcome suggests that our screening threshold is excessively conservative at those frequencies and that a more precise screening threshold may be frequency dependent. For example, it might take into account the f^{-2} character of the noise in $S\{\mathbf{u}_\mathbf{a}\}$ (Fig. 6). For the purpose of this work, the $S\{\mathbf{u}_h\}/S\{\mathbf{u}\} < 3$ threshold for spectral fits is sufficient, and detailed characterization of the IMU's motion- and frequency-dependent noise level is left for future work.

c. *StableMoor spectra*

Spectra of SMB motion have broader peaks, with a maximum amplitude that is approximately half the frequency of the TTM spectral peak (0.06 Hz; Fig. 10). The motion of this platform also does not have high-frequency ''subpeaks'' or other high-frequency broadband excitation (Part I). These characteristics are due to the more massive and hydrodynamically streamlined properties of the SMB compared to the TTM.

Like the TTM, the motion-corrected spectra from the SMB are consistent with turbulence theory and previous observations. A notable distinction from the TTM, however, is that there are no obvious persistent motion contamination peaks. That is, this measurement system provides an accurate estimate of the turbulence spectra at this location from low frequencies to more than 1 Hz—well into the inertial subrange—for all three components of velocity.

Note that this level of accuracy cannot be obtained without the independent estimate of $\mathbf{u}_{\mathrm{low}}$ (from the bottom-tracking ADP). If we assume that $\mathbf{u}_{\mathrm{low}} = 0$, then a similar plot to Fig. 10 (not shown) reveals persistent motion-contamination peaks and troughs in $S\{u\}$ and $S\{v\}$ regardless of the choice of $f_\mathbf{a}$. This indicates that the low-frequency translational motion of the SMB that is important to motion correction is poorly resolved by the IMU's accelerometer. In other words, compared to the TTM, the SMB provides a more

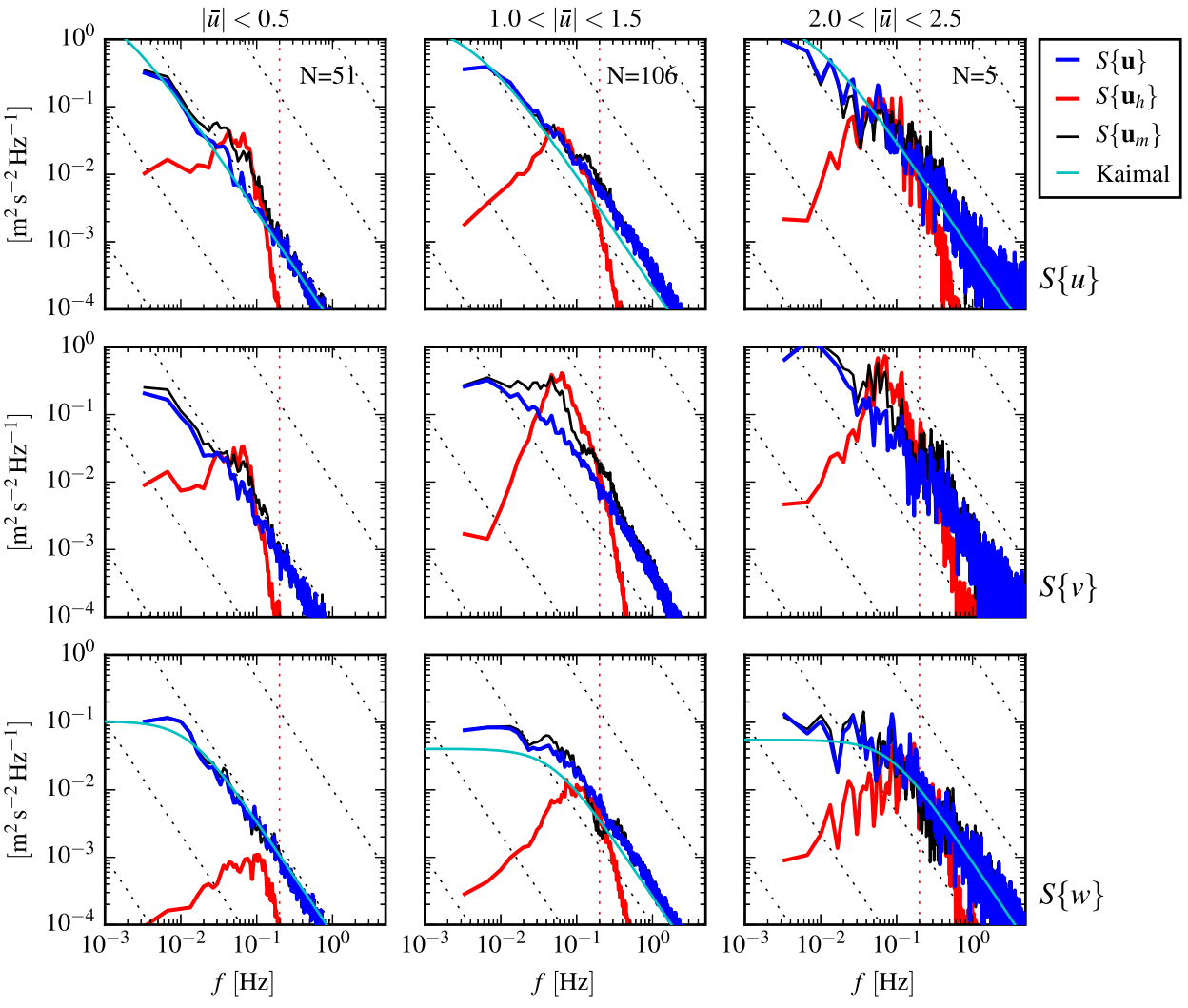

FIG. 10. Turbulence spectra from the SMB. The axes layout and annotations are identical to Fig. 9, except that $S\{\mathbf{u}_h\}$ is plotted as a solid line at all frequencies because it is measured at all frequencies.

accurate measurement of turbulence when it includes an independent measure of $\mathbf{u}_{\mathrm{low}}$, but it does no better—and perhaps worse—when it does not.

d. Torpedo spectra

Terms $S\{u_h\}$ and $S\{v_h\}$ for the turbulence torpedo are broadband and $S\{w_h\}$ motion has a narrow peak at 0.3 Hz (Fig. 11). Because $\mathbf{u}_h$ is estimated using $f_{\mathbf{a}} = 0.03$ Hz and assuming $\mathbf{u}_{\mathrm{low}} = 0$, its spectra roll off quickly below $f_{\mathbf{a}}$. Motion correction of the torpedo data appears to effectively remove a motion peak from $S\{w\}$ at 0.3 Hz, and corrects $S\{v\}$ between 0.04 and 0.6 Hz. Term $S\{u\}$ is mostly unaffected by motion at these frequencies, because the torpedo motion is smaller than the turbulence in this direction. At frequencies below $f_{\mathbf{a}}$, $S\{u\}$ and $S\{v\}$ increase dramatically. This suggests that unresolved low-frequency motion of the torpedo is contaminating the velocity measurements at these frequencies. It may be possible to correct for some of this contamination using a measurement of the ship's motion as a proxy for the torpedo's low-frequency motion, but this has not been done. Still, above $f_{\mathbf{a}}$ the torpedo appears to provide a reliable estimate of spectral amplitude in the inertial subrange and can therefore be used to estimate ε. Considering the simplicity of the platform, it may be a useful option for quantifying this turbulence statistic in a variety of scenarios. If a GPS is positioned above it, it may be capable of providing even more.

e. Cross spectra

Cross spectra indicate the correlation between different velocity components as a function of frequency, and their integrals are the Reynolds stresses. Head

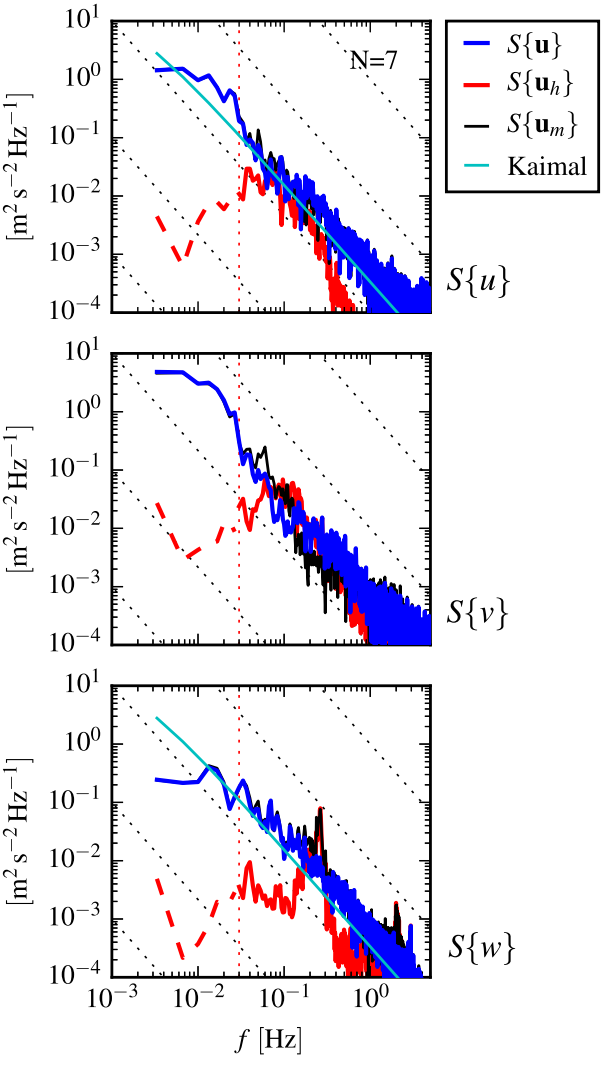

FIG. 11. Turbulence spectra from the turbulence torpedo during a 35-min period when the mean velocity was 1.3 m s^{-1}. Annotations and line colors are identical to Fig. 9.

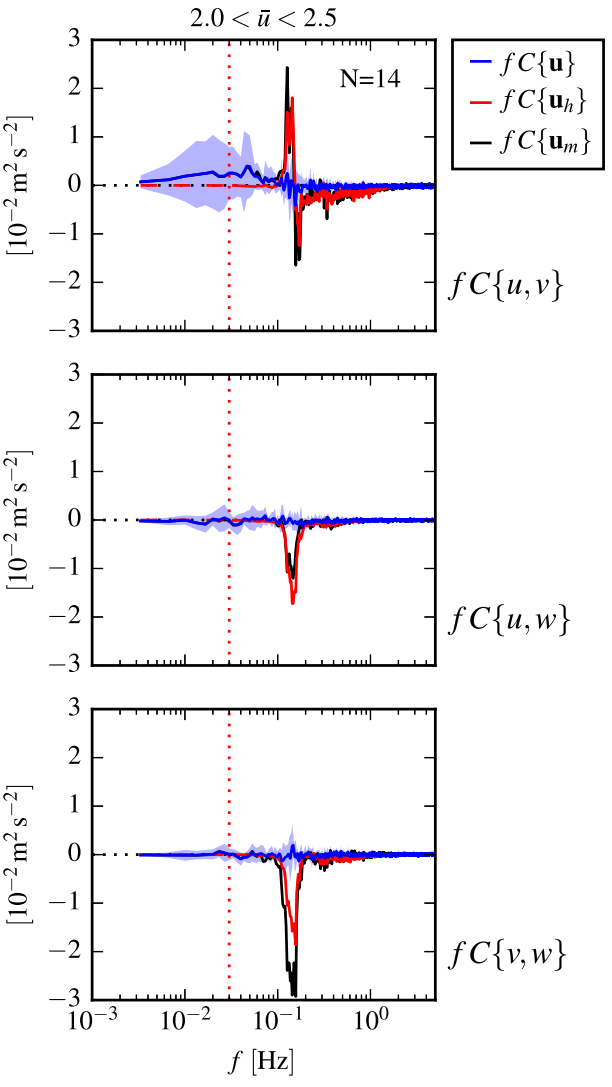

FIG. 12. Variance-preserving cross spectra between components of $\mathbf{u}$ (blue), $\mathbf{u}_h$ (red), and $\mathbf{u}_m$ (black) from the June 2014 TTM deployment: (top) $fC\{u, v\}$, (middle) $fC\{u, w\}$, and (bottom) $fC\{v, w\}$ (also indicated at right). Note that these cross spectra are between components of a velocity vector (e.g., $\mathbf{u}$), not between different vectors (i.e., not between $\mathbf{u}$ and $\mathbf{u}_m$). Term N is the number of spectral ensembles in this average, i.e., when $2 < |u| < 2.5$ m s^{-1}. The light blue shading indicates one standard deviation of $fC\{\mathbf{u}\}$.

motion cross spectra $C\{\mathbf{u}_h\}$ (Fig. 12, red) and uncorrected velocity cross spectra $C\{u_m\}$ (black) from TTM measurements have large peaks at the same frequency (0.15 Hz) as peaks in autospectra (Fig. 9). This indicates that mooring motion contaminates the uncorrected cross-spectral velocity measurements and that Reynolds stress estimates based on uncorrected velocity measurements will be contaminated by mooring motion.

Fortunately, motion-corrected velocity cross spectra $C\{\mathbf{u}\}$ (Fig. 12, blue) have reduced cross-spectral amplitudes at these frequencies. This indicates that motion correction reduces motion contamination to produce more reliable estimates of velocity cross spectra and Reynolds stresses (Fig. 12). Notably, the low standard deviation of $fC\{\mathbf{u}\}$ (indicated by the blue shading) compared to the mean values of $fC\{\mathbf{u}_h\}$ and $fC\{\mathbf{u}_m\}$—at the frequencies of maximum motion—indicates that even the individual values of $C\{\mathbf{u}\}$ are reduced at these frequencies, compared to $C\{\mathbf{u}_m\}$, not just their mean.

These results indicate that motion-corrected TTM velocity measurements can be used to estimate turbulence Reynolds stresses. Without motion correction, Reynolds stress estimates would be contaminated by the large peaks in the cross spectra that are caused by the swaying and fluttering motion of the TTM vane. Cross-spectra of TTM data for other velocity ranges (i.e., <2 m s^{-1}), and cross spectra from the SMB show similar results (not

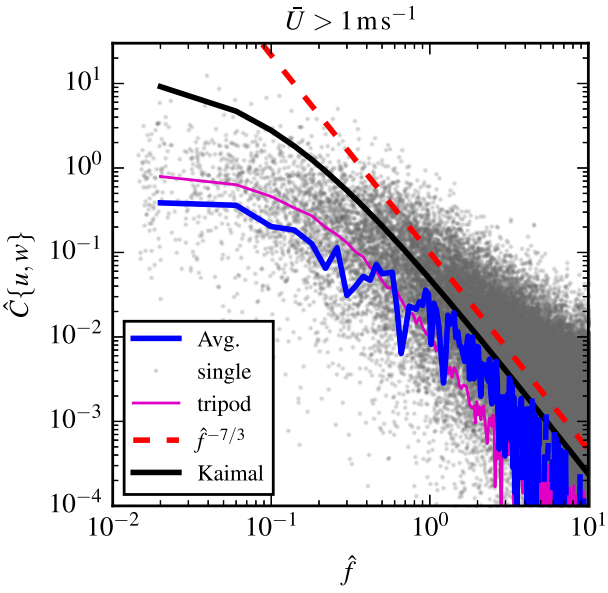

FIG. 13. Nondimensional cross spectra of motion corrected velocity $\hat{C}\{u, w\}$ on a log–log scale. The average over $\Delta\hat{f} = 0.04$ bins is shown in blue, and single points are gray (negative values not shown). The semiempirical Kaimal et al. (1972) form is shown as a thick black line, and the red dashed line indicates an $\hat{f}^{-7/3}$ slope. Cross-spectral estimates from measurements from a fixed tripod are in purple.

shown). However, we note that because the SMB is less stable in pitch than the TTM (see Part I for details), the TTM provides more accurate estimates of $\overline{uw}$.

To compare the cross spectra to other measurements, we normalize them following Kaimal et al. (1972) as $\hat{C}\{u, w\}(\hat{f}) = -C\{u, w\}f_\circ/u_*^2$, where $f_\circ = \overline{U}/z$ and $\hat{f} = f/f_\circ$. When plotted on a log–log scale, $\hat{C}\{u, w\}$ has an $\hat{f}^{-7/3}$ high-frequency spectral slope that is consistent with other measurements (Fig. 13). At low frequency, the cross spectra are more than 10 times smaller than the semiempirical Kaimal form, but this discrepancy is consistent with other measurements of cross spectra. In particular, Walter et al. (2011) observed a half-decade reduction from the Kaimal form near the seafloor, and measurements from an ADV positioned 4.6 m above the seafloor on a fixed tripod at a different site in Puget Sound show a similar degree of deviation as observed here (Thomson et al. 2012).

While one might be inclined to attribute the discrepancy between these estimates and the Kaimal form to normalization by local u_*, the agreement between autospectra and their Kaimal form suggests otherwise (Fig. 9). Instead, we conclude that either the Kaimal cross spectra do not apply universally at distances far from the bottom boundary or the spectra are being modified by physics other than bottom boundary layer–driven turbulence. Either way, the agreement of TTM-measured cross spectra with measurements from stationary platforms is interpreted as an indication that this platform can resolve cross spectra and Reynolds stresses.

5. Discussion

Ideally, moored motion-corrected turbulence velocity measurements would be validated against simultaneous independent validated measurements of turbulence velocity at the same scales, time, and location. Accomplishing this, however, involves significant technical challenges that are not easily overcome—most notably the difficulty of measuring turbulence at the same point as the moving ADV. A slightly less ideal but much more realistic confirmation of the methodology might involve comparing the statistics of moored turbulence measurements to those from a nearby fixed platform, or a fixed platform placed at the same location at a different time (e.g., the "tripod" platform described in Thomson et al. 2012). Unfortunately, to our knowledge these measurements have not yet been made.

The previous section showed that the shape of the turbulence velocity spectra from moored ADVs is consistent with Kolmogorov's theory of locally isotropic turbulence, which has been observed consistently in turbulence measurements for decades (Kolmogorov 1941; Grant et al. 1962; McMillan et al. 2016). This is interpreted as the first indication that the measurement systems presented are capable of accurately resolving turbulence. The degree to which uncorrected spectra were corrected toward this theoretical and observationally confirmed shape is interpreted as a measure of the improvement of the spectral estimates by motion correction. This section takes that reasoning one step further to demonstrate that motion-corrected velocity measurements can produce estimates of turbulence statistics that are consistent with the physical processes that can be reasonably assumed to dominate the measurement site.

Figure 14 presents a time series of the mean velocity (Fig. 14a) and several turbulence statistics that were measured during the June 2014 TTM deployment. This figure shows the evolution of the flow through Admiralty Inlet during 1.5 tidal cycles. The TKE (Fig. 14b), Reynolds stresses (Fig. 14c), dissipation, and one component of turbulence production (Fig. 14d) grow and strengthen with ebb or flood and then subside during slack tide. This component of turbulence production is calculated using

$$P_{uz} = \overline{uw}\frac{\partial\overline{u}}{\partial z}, \tag{4}$$

where $\partial\overline{u}/\partial z$ is computed from the two ADVs on the TTM. The highest values of ε and P_{uz} occur at the peak of the ebb or flood, which is in agreement with other

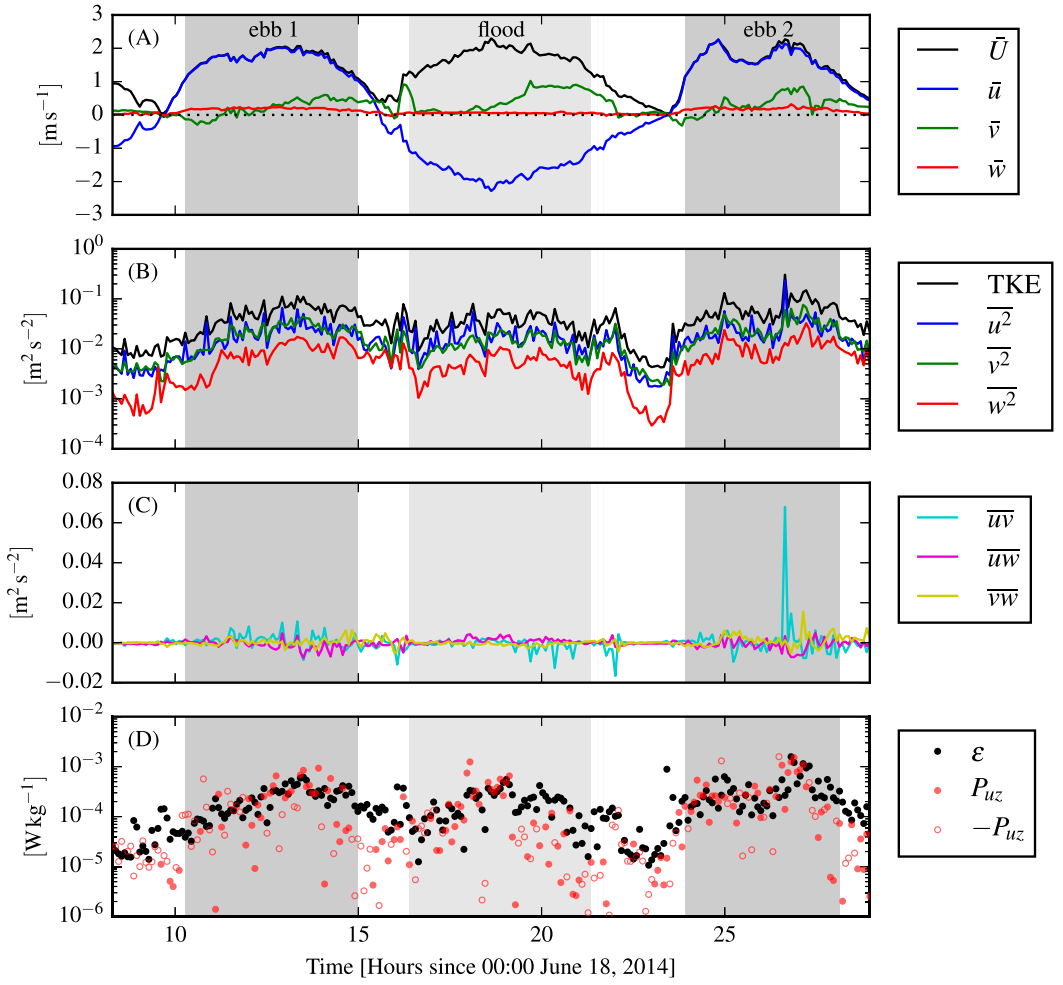

FIG. 14. (a) Time series of mean velocities, (b) turbulence energy and its components, (c) Reynolds stresses, and (d) turbulence dissipation rate measured by the TTM during the June 2014 deployment. Shading indicates periods of ebb ($\overline{u} > 1.0\,\mathrm{m\,s^{-1}}$, gray) and flood ($\overline{u} < -1.0\,\mathrm{m\,s^{-1}}$, lighter gray).

measurements in tidal channels. The agreement of the magnitude of P_{uz} with ε at those times suggests a local production–dissipation balance that is often observed in tidally forced channels (Trowbridge et al. 1999; Stacey et al. 1999b; McMillan et al. 2016). At other times, the value of P_{uz} is insufficient to balance ε or is negative.

Inspection of the negative P_{uz} values reveals that most of them are caused by a reversed sign of $\overline{uw}$ rather than a reversed sign of $\partial u/\partial z$ (i.e., when compared to the sign of u). This finding suggests that uncertainty in $\overline{uw}$ may be contributing to discrepancies between P_{uz} and ε. Furthermore, considering the complex nature of the bathymetry and shoreline at this site (i.e., the headland), it is not surprising that P_{uz} does not perfectly balance ε. Other terms of the TKE equation are likely to be important, such as turbulence advection, other components of production, and turbulent transport. The fact that P_{uz} and ε are in near balance as often as they are indicates that bottom boundary layer physics are important to the turbulence dynamics at this site.

Given the assumptions implicit in this comparison and the discussion above, agreement between P_{uz} and ε—especially for the highest values of ε—suggests the turbulent boundary layer reaches the depth of these measurements (10 m) during the highest flow speeds (Fig. 15). This result is further supported by a comparison of $\overline{U}$ with ε (Fig. 16). Here we see a $\varepsilon \propto \overline{U}^3$ dependence that is again suggestive of bottom boundary layer physics (Trowbridge 1992; Nash et al. 2009). At lower flow speeds, ε deviates from this relationship, which suggests that the boundary layer is no longer the dominant physical process at the depth of these measurements.

There are two intriguing differences between the ebb and flood datasets: 1) the drag coefficient relating ε to $\overline{U}^3$

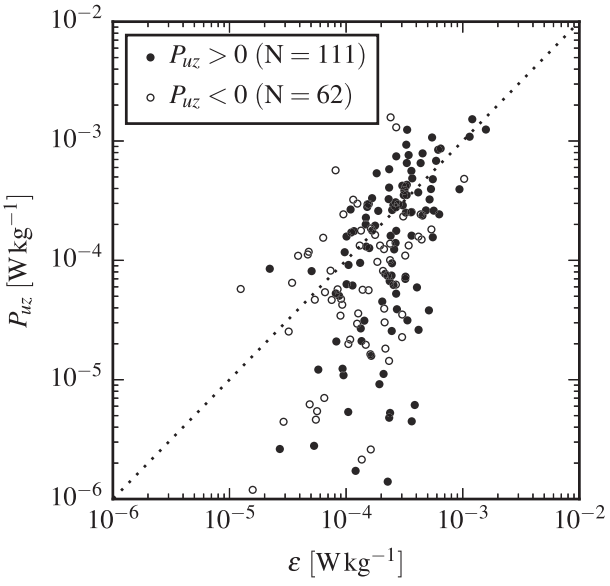

FIG. 15. Term P_{uz} vs ε during the June 2014 TTM deployment for values of $|u| > 1$ m s^{-1}. Values of negative production are indicated as open circles.

is larger for ebbs and 2) the fit does not hold as well for low flow speeds (Fig. 16). These details are not surprising considering the complex bathymetry at the test site (Fig. 1). In particular, the flow immediately upstream of the measurement site is exposed to much more bathymetric curvature—that is, from the headland—during ebb (when $\overline{u}$ is >0) than the during flood ($\overline{u} < 0$). Based on this, one might expect flow separation (turbulence advection), turbulence production, or turbulence transport emanating from the headland to have a stronger impact on the flow at this site during ebb than flood. These effects are a likely contributor to the distinct relationships observed in Fig. 16.

The hypothesis that the headland is a key contributor to the turbulence dynamics at this site suggests that terms such as cross-stream turbulence advection $\overline{v}\partial\text{TKE}/\partial y$, the lateral turbulent transport terms $\partial\overline{u_i u_i v}/\partial y$, or lateral shear production $\overline{uv}\partial\overline{u}/\partial y$ may contribute significantly to the dynamics of turbulence at this site. While we did not measure stratification profiles during these measurements, we do not typically expect buoyancy flux to play a dominant role because this region tends to be tidally well mixed (Geyer and Cannon 1982). In summary, bottom boundary layer physics seems to be the dominant process at the measurement site, with lateral advection, lateral transport, and lateral production of TKE also potentially contributing—especially during ebb. A more detailed analysis of the turbulence and momentum dynamics of this headland is left for future work [e.g., similar to Warner et al. (2013)].

6. Conclusions

This work presents a methodology for measuring turbulence from moored ADV-IMUs and demonstrates that motion correction reduces mooring motion contamination. A comparison of spectra of ADV head motion $S\{\mathbf{u}_h\}$ to that of motion-corrected $S\{\mathbf{u}\}$ and uncorrected spectra $S\{\mathbf{u}_m\}$ reveals that motion correction improves spectral estimates of moored ADV

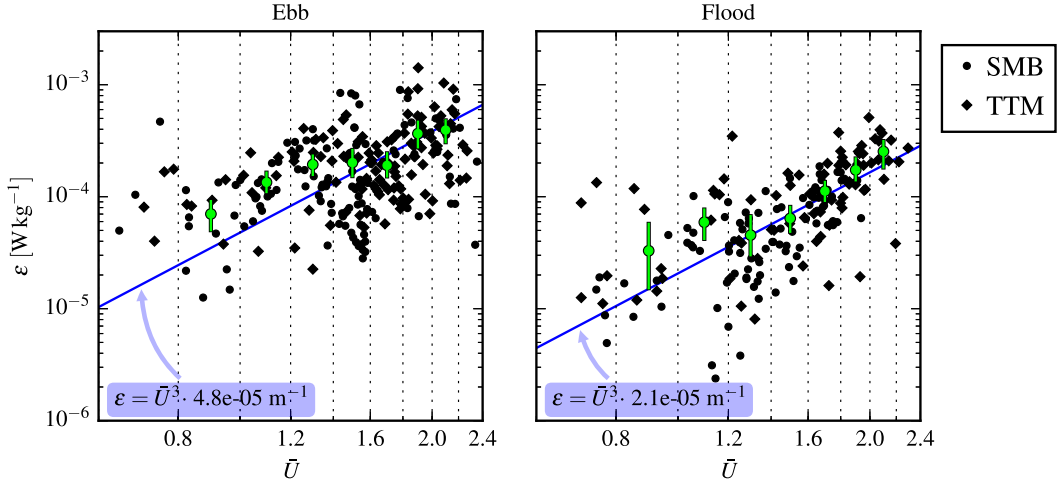

FIG. 16. A log–log plot of ε vs $\overline{U}$ for the June 2014 TTM (diamonds) and May 2015 SMB (dots) deployments, during (left) ebb and (right) flood. Black points are 5-min averages. Green dots are mean values within speed bins of 0.2 m s^{-1} width that have at least 10 points (50 min of data); their vertical bars are 95% bootstrap confidence intervals. The blue line shows a $\overline{U}^3$ slope, wherein the proportionality constant (blue box) is calculated by taking the log-space mean of $\varepsilon/\overline{U}^3$.

measurements. In particular, we found that motion-corrected spectra have spectral shapes that are similar to previous measurements of tidal-channel turbulence and have $f^{-5/3}$ spectral slopes at high frequencies. This finding suggests that the motion-corrected spectra resolve the inertial subrange predicted by Kolmogorov's theory of locally isotropic turbulence.

Motion correction reduces motion contamination for all platforms we presented, but it does not necessarily remove it completely. This outcome seems to depend on the relative amplitude of platform motion compared to the underlying turbulence being measured. The most notable example of this is from TTM $S\{v\}$, which have large-amplitude "swaying" peaks at 0.15 Hz that interrupt the frequently observed rolloff between the low-frequency "energy-containing scales" and the $f^{-5/3}$ inertial subrange.

The possibility of persistent motion contamination requires that motion-corrected turbulence measurements from moored ADV-IMUs be interpreted with care. An inspection of spectra presented here suggests that excluding spectral regions where $S\{\mathbf{u}_h\}/S\{\mathbf{u}\} > 3$ removes persistent motion contamination peaks while still preserving spectral regions where motion correction is effective. Using this criteria, it is then possible to produce spectral fits that exclude persistent motion contamination and to provide reliable estimates of turbulence quantities of interest (e.g., ε and TKE).

We have also shown that motion correction reduces motion contamination in cross spectra. This finding is important because it suggests that moored ADV-IMU measurements may be used to produce reliable estimates of Reynolds stresses. We utilized these stress estimates and vertical shear estimates, both from the TTM, to estimate P_{uz}.

Finally, we have shown that ε estimates based on motion-corrected spectra scale with $\overline{U}^3$ and balance P_{uz} estimates during peak ebb and flood. Together, these results indicate that bottom boundary layer physics are a dominant process at this site, and that the boundary layer reaches the height of the ADV-IMUs (10 m) during ebb and flood. The degree of agreement between P_{uz} and ε also serves as an indicator of the self-consistency of moored ADV-IMU turbulence measurements.

Acknowledgments. Many thanks are given to Joe Talbert, Alex DeKlerk, Captain Andy Reay-Ellers, Jennifer Rinker, Maricarmen Guerra, and Eric Nelson in assisting with data collection. The authors are also grateful to James VanZwieten, Matthew Egeland, and Marshall Richmond for discussion on the details of this work.

Thanks are given to the open-source software community for the tools used in this work, especially the developers of LATEX, Python, NumPy, MatPlotLib, git, and GNU Emacs.

This work was supported by the U.S. Department of Energy under Contract DE-AC36-08GO28308 with the National Renewable Energy Laboratory. Funding for the work was provided by the DOE's Office of Energy Efficiency and Renewable Energy and Wind and Water Power Technologies Office.

REFERENCES

Afgan, I., J. McNaughton, S. Rolfo, D. Apsley, T. Stallard, and P. Stansby, 2013: Turbulent flow and loading on a tidal stream turbine by LES and RANS. *Int. J. Heat Fluid Flow*, **43**, 96–108, doi:10.1016/j.ijheatfluidflow.2013.03.010.

Alexander, S. R., and P. E. Hamlington, 2015: Analysis of turbulent bending moments in tidal current boundary layers. *J. Renewable Sustainable Energy*, **7**, 063118, doi:10.1063/1.4936287.

Alford, M. H., 2010: Sustained, full-water-column observations of internal waves and mixing near Mendocino Escarpment. *J. Phys. Oceanogr.*, **40**, 2643–2660, doi:10.1175/2010JPO4502.1.

Axford, D., 1968: On the accuracy of wind measurements using an inertial platform in an aircraft, and an example of a measurement of the vertical mesostructure of the atmosphere. *J. Appl. Meteor.*, **7**, 645–666, doi:10.1175/1520-0450(1968)007<0645:OTAOWM>2.0.CO;2.

Barshan, B., and H. F. Durrant-Whyte, 1995: Inertial navigation systems for mobile robots. *IEEE Trans. Robot. Autom.*, **11**, 328–342, doi:10.1109/70.388775.

Bevly, D. M., 2004: Global positioning system (GPS): A low-cost velocity sensor for correcting inertial sensor errors on ground vehicles. *J. Dyn. Syst. Meas. Control*, **126**, 255–264, doi:10.1115/1.1766027.

Cartwright, G. M., C. T. Friedrichs, P. J. Dickhudt, T. Gass, and F. H. Farmer, 2009: Using the Acoustic Doppler Velocimeter (ADV) in the MUDBED real-time observing system. *OCEANS 2009: MTS/IEEE Bioloxi; Marine Technology for Our Future: Global and Local Challenges*, IEEE, 1–9, doi:10.23919/OCEANS.2009.5422146.

Doherty, K., D. Frye, S. Liberatore, and J. Toole, 1999: A moored profiling instrument. *J. Atmos. Oceanic Technol.*, **16**, 1816–1829, doi:10.1175/1520-0426(1999)016<1816:AMPI>2.0.CO;2.

Edson, J. B., A. A. Hinton, K. E. Prada, J. E. Hare, and C. W. Fairall, 1998: Direct covariance flux estimates from mobile platforms at sea. *J. Atmos. Oceanic Technol.*, **15**, 547–562, doi:10.1175/1520-0426(1998)015<0547:DCFEFM>2.0.CO;2.

Egeland, M. N., 2014: Spectral evaluation of motion compensated ADV systems for ocean turbulence measurements. M.S. thesis, Dept. of Ocean and Mechanical Engineering, Florida Atlantic University, 82 pp.

Fer, I., and M. B. Paskyabi, 2014: Autonomous ocean turbulence measurements using shear probes on a moored instrument. *J. Atmos. Oceanic Technol.*, **31**, 474–490, doi:10.1175/JTECH-D-13-00096.1.

Finlayson, D., 2005: Combined bathymetry and topography of the Puget Lowlands. School of Oceanography, University of Washington, accessed 1 September 2014 (file g1230485.zip). [Available online at https://www.ocean.washington.edu/data/pugetsound/psdem2005.html.]

Geyer, W. R., and G. A. Cannon, 1982: Sill processes related to deep water renewal in a fjord. *J. Geophys. Res.*, **87**, 7985–7996, doi:10.1029/JC087iC10p07985.

——, M. E. Scully, and D. K. Ralston, 2008: Quantifying vertical mixing in estuaries. *Environ. Fluid Mech.*, **8**, 495–509, doi:10.1007/s10652-008-9107-2.

Goodman, L., E. R. Levine, and R. G. Lueck, 2006: On measuring the terms of the turbulent kinetic energy budget from an AUV. *J. Atmos. Oceanic Technol.*, **23**, 977–990, doi:10.1175/JTECH1889.1.

Grant, H. L., R. W. Stewart, and A. Moilliet, 1962: Turbulence spectra from a tidal channel. *J. Fluid Mech.*, **12**, 241–263, doi:10.1017/S002211206200018X.

Guerra Paris, M., and J. Thomson, 2017: Turbulence measurements from five-beam acoustic Doppler current profilers. *J. Atmos. Oceanic Technol.*, **34**, 1267–1284, doi:10.1175/JTECH-D-16-0148.1.

Gulmammadov, F., 2009: Analysis, modeling and compensation of bias drift in MEMS inertial sensors. *RAST'09: Fourth International Conference on Recent Advances in Space Technologies, 2009*, IEEE, 591–596, doi:10.1109/RAST.2009.5158260.

Gunawan, B., V. S. Neary, and J. Colby, 2014: Tidal energy site resource assessment in the East River tidal strait, near Roosevelt Island, New York, NY. *Renewable Energy*, **71**, 509–517, doi:10.1016/j.renene.2014.06.002.

Hand, M. M., N. D. Kelley, and M. J. Balas, 2003: Identification of wind turbine response to turbulent inflow structures. National Renewable Energy Laboratory Conf. Paper NREL/CP-500-33465, 10 pp.

Harding, S., L. Kilcher, and J. Thomson, 2017: Turbulence measurements from compliant moorings. Part I: Motion characterization. *J. Atmos. Oceanic Technol.*, **34**, 1235–1247, doi:10.1175/JTECH-D-16-0189.1.

Kaimal, J. C., J. C. Wyngaard, Y. Izumi, and O. R. Cote, 1972: Spectral characteristics of surface-layer turbulence. *Quart. J. Roy. Meteor. Soc.*, **98**, 563–589, doi:10.1002/qj.49709841707.

Kelley, N. D., B. J. Jonkman, G. N. Scott, J. T. Bialasiewicz, and L. S. Redmond, 2005: The impact of coherent turbulence on wind turbine aeroelastic response and its simulation. National Renewable Energy Laboratory Conf. Paper NREL/CP-500-38074, 19 pp.

Kilcher, L., J. Thomson, J. Talbert, and A. DeKlerk, 2016: Measuring turbulence from moored acoustic Doppler velocimeters: A manual to quantifying inflow at tidal energy sites. National Renewable Energy Laboratory Tech. Rep. NREL/TP-5000-62979, 34 pp. [Available online at www.nrel.gov/docs/fy16osti/62979.pdf.]

——, ——, and S. Harding, 2017: Admiralty Inlet advanced turbulence measurements: Final data and code archive. Accessed 7 February 2017. [Available online at http://mhkdr.openei.org/submissions/223.]

Kim, S.-C., C. T. Friedrichs, J. P.-Y. Maa, and L. D. Wright, 2000: Estimating bottom stress in tidal boundary layer from acoustic Doppler velocimeter data. *J. Hydraul. Eng.*, **126**, 399–406, doi:10.1061/(ASCE)0733-9429(2000)126:6(399).

Kolmogorov, A. N., 1941: Dissipation of energy in the locally isotropic turbulence. *Dokl. Akad. Nauk SSSR*, **32**, 16–18. [Available online at http://www.jstor.org/stable/51981.]

Kraus, N. C., A. Lohrmann, and R. Cabrera, 1994: A new acoustic meter for measuring 3D laboratory flows. *J. Hydraul. Eng.*, **120**, 406–412, doi:10.1061/(ASCE)0733-9429(1994)120:3(406).

Lohrmann, A., R. Cabrera, G. Gelfenbaum, and J. Haines, 1995: Direct measurements of Reynolds stress with an acoustic Doppler velocimeter. *Proceedings of the IEEE Fifth Working Conference on Current Measurement*, S. P. Anderson, G. F. Appell, and A. J. Williams III, Eds., IEEE, 205–210, doi:10.1109/CCM.1995.516175.

Lorke, A., 2007: Boundary mixing in the thermocline of a large lake. *J. Geophys. Res.*, **112**, C09019, doi:10.1029/2006JC004008.

Lueck, R. G., and D. Huang, 1999: Dissipation measurement with a moored instrument in a swift tidal channel. *J. Atmos. Oceanic Technol.*, **16**, 1499–1505, doi:10.1175/1520-0426(1999)016<1499:DMWAMI>2.0.CO;2.

Lumley, J., and E. Terray, 1983: Kinematics of turbulence convected by a random wave field. *J. Phys. Oceanogr.*, **13**, 2000–2007, doi:10.1175/1520-0485(1983)013<2000:KOTCBA>2.0.CO;2.

McCaffrey, K., B. Fox-Kemper, P. E. Hamlington, and J. Thomson, 2015: Characterization of turbulence anisotropy, coherence, and intermittency at a prospective tidal energy site: Observational data analysis. *Renewable Energy*, **76**, 441–453, doi:10.1016/j.renene.2014.11.063.

McMillan, J. M., A. E. Hay, R. G. Lueck, and F. Wolk, 2016: Rates of dissipation of turbulent kinetic energy in a high Reynolds number tidal channel. *J. Atmos. Oceanic Technol.*, **33**, 817–837, doi:10.1175/JTECH-D-15-0167.1.

MicroStrain, 2010: 3DM-GX3-25: Coning and sculling. Revision 2.0, Tech. Rep. I0019, 2 pp. [Available online at http://files.microstrain.com/TN-I0019_3DM-GX3-25__Coning_And_Sculling.pdf.]

——, 2012: 3DM-GX3-15, 3DM-GX3-25 MIP data communications protocol. Revision 002, DCP Manual 8500-0024, 90 pp. [Available online at http://files.microstrain.com/3DM-GX3-15-25-MIP-Data-Communications-Protocol.pdf.]

Miller, S. D., T. S. Hristov, J. B. Edson, and C. A. Friehe, 2008: Platform motion effects on measurements of turbulence and air–sea exchange over the open ocean. *J. Atmos. Oceanic Technol.*, **25**, 1683–1694, doi:10.1175/2008JTECHO547.1.

Morison, J. R., J. W. Johnson, and S. A. Schaaf, 1950: The force exerted by surface waves on piles. *J. Pet. Technol.*, **2**, 149–154, doi:10.2118/950149-G.

Moum, J., and J. Nash, 2009: Mixing measurements on an equatorial ocean mooring. *J. Atmos. Oceanic Technol.*, **26**, 317–336, doi:10.1175/2008JTECHO617.1.

Mücke, T., D. Kleinhans, and J. Peinke, 2011: Atmospheric turbulence and its influence on the alternating loads on wind turbines. *Wind Energy*, **14**, 301–316, doi:10.1002/we.422.

Nash, J. D., E. Kunze, J. M. Toole, and R. W. Schmitt, 2004: Internal tide reflection and turbulent mixing on the continental slope. *J. Phys. Oceanogr.*, **34**, 1117–1134, doi:10.1175/1520-0485(2004)034<1117:ITRATM>2.0.CO;2.

——, L. F. Kilcher, and J. N. Moum, 2009: Structure and composition of a strongly stratified, tidally pulsed river plume. *J. Geophys. Res.*, **114**, C00B12, doi:10.1029/2008JC005036.

Nortek, 2005: Vector current meter. Revision H, Nortek AS User Manual N300-100, 84 pp.

Paskyabi, M. B., and I. Fer, 2013: Turbulence measurements in shallow water from a subsurface moored moving platform. *Energy Procedia*, **35**, 307–316, doi:10.1016/j.egypro.2013.07.183.

Perlin, A., and J. N. Moum, 2012: Comparison of thermal variance dissipation rates from moored and profiling instruments at the equator. *J. Atmos. Oceanic Technol.*, **29**, 1347–1362, doi:10.1175/JTECH-D-12-00019.1.

Polagye, B., and J. Thomson, 2013: Tidal energy resource characterization: Methodology and field study in Admiralty Inlet, Puget Sound, WA (USA). *J. Power Energy*, **227A**, 352–367, doi:10.1177/0957650912470081.

Rippeth, T. P., E. Williams, and J. H. Simpson, 2002: Reynolds stress and turbulent energy production in a tidal channel. *J. Phys. Oceanogr.*, **32**, 1242–1251, doi:10.1175/1520-0485(2002)032<1242:RSATEP>2.0.CO;2.

Sreenivasan, K. R., 1995: On the universality of the Kolmogorov constant. *Phys. Fluids*, **7**, 2778–2784, doi:10.1063/1.868656.

Stacey, M. T., S. G. Monismith, and J. R. Burau, 1999a: Measurements of Reynolds stress profiles in unstratified tidal flow. *J. Geophys. Res.*, **104**, 10 933–10 949, doi:10.1029/1998JC900095.

——, ——, and ——, 1999b: Observations of turbulence in a partially stratified estuary. *J. Phys. Oceanogr.*, **29**, 1950–1970, doi:10.1175/1520-0485(1999)029<1950:OOTIAP>2.0.CO;2.

Thomson, J., B. Polagye, V. Durgesh, and M. Richmond, 2012: Measurements of turbulence at two tidal energy sites in Puget Sound, WA. *J. Oceanic Eng.*, **37**, 363–374, doi:10.1109/JOE.2012.2191656.

Trowbridge, J. H., 1992: A simple description of the deepening and structure of a stably stratified flow driven by a surface stress. *J. Geophys. Res.*, **97**, 15 529–15 543, doi:10.1029/92JC01512.

——, W. R. Geyer, M. M. Bowen, and A. J. I. Williams, 1999: Near-bottom turbulence measurements in a partially mixed estuary: Turbulent energy balance, velocity structure and along-channel momentum balance. *J. Phys. Oceanogr.*, **29**, 3056–3072, doi:10.1175/1520-0485(1999)029<3056:NBTMIA>2.0.CO;2.

van der Walt, S., S. C. Colbert, and G. Varoquaux, 2011: The NumPy array: A structure for efficient numerical computation. *Comput. Sci. Eng.*, **13**, 22–30, doi:10.1109/MCSE.2011.37.

VanZwieten, J. H., M. N. Egeland, K. D. von Ellenrieder, J. W. Lovenbury, and L. Kilcher, 2015: Experimental evaluation of motion compensated ADV measurements for in-stream hydrokinetic applications. *2015 IEEE/OES Eleventh Current, Waves and Turbulence Measurement (CWTM)*, IEEE, 1–8, doi:10.1109/CWTM.2015.7098119.

Voulgaris, G., and J. H. Trowbridge, 1998: Evaluation of the acoustic Doppler velocimeter (ADV) for turbulence measurements. *J. Atmos. Oceanic Technol.*, **15**, 272–289, doi:10.1175/1520-0426(1998)015<0272:EOTADV>2.0.CO;2.

Walter, R. K., N. J. Nidzieko, and S. G. Monismith, 2011: Similarity scaling of turbulence spectra and cospectra in a shallow tidal flow. *J. Geophys. Res.*, **116**, C10019, doi:10.1029/2011JC007144.

Warner, S. J., P. MacCready, J. N. Moum, and J. D. Nash, 2013: Measurement of tidal form drag using seafloor pressure sensors. *J. Phys. Oceanogr.*, **43**, 1150–1172, doi:10.1175/JPO-D-12-0163.1.

Wiles, P. J., T. P. Rippeth, J. H. Simpson, and P. J. Hendricks, 2006: A novel technique for measuring the rate of turbulent dissipation in the marine environment. *Geophys. Res. Lett.*, **33**, L21608, doi:10.1029/2006GL027050.

Winkel, D., M. Gregg, and T. Sanford, 1996: Resolving oceanic shear and velocity with the multi-scale profiler. *J. Atmos. Oceanic Technol.*, **13**, 1046–1072, doi:10.1175/1520-0426(1996)013<1046:ROSAVW>2.0.CO;2.

Wyngaard, J. C., L. Rockwell, and C. A. Friehe, 1985: Errors in the measurement of turbulence upstream of an axisymmetric body. *J. Atmos. Oceanic Technol.*, **2**, 605–614, doi:10.1175/1520-0426(1985)002<0605:EITMOT>2.0.CO;2.

Zhang, Y., K. Streitlien, J. G. Bellingham, and A. B. Baggeroer, 2001: Acoustic Doppler velocimeter flow measurement from an autonomous underwater vehicle with applications to deep ocean convection. *J. Atmos. Oceanic Technol.*, **18**, 2038–2051, doi:10.1175/1520-0426(2001)018<2038:ADVFMF>2.0.CO;2.